



PCCP

Time-Resolved Photoionization Spectroscopy of Mixed Rydberg-Valence States: Indole Case Study

Journal:	<i>Physical Chemistry Chemical Physics</i>
Manuscript ID	CP-ART-08-2015-004645.R2
Article Type:	Paper
Date Submitted by the Author:	09-Sep-2015
Complete List of Authors:	Zawadzki, Magdalena; Heriot-Watt University, Institute of Photonics & Quantum Sciences Thompson, James; Heriot-Watt University, Institute of Photonics & Quantum Sciences Burgess, Emma; Heriot-Watt University, Institute of Photonics & Quantum Sciences Paterson, Martin; Heriot-Watt University, Institute Of Chemical Sciences Townsend, David; Heriot-Watt University, Institute of Photonics & Quantum Sciences

SCHOLARONE™
Manuscripts

Time-Resolved Photoionization Spectroscopy of Mixed Rydberg-Valence States: Indole Case Study

Magdalena M. Zawadzki¹, James O. F. Thompson^{1,a}, Emma A. Burgess¹, Martin J. Paterson² and Dave Townsend^{1,2,b}

¹ *Institute of Photonics & Quantum Sciences, Heriot-Watt University, Edinburgh, EH14 4AS, United Kingdom*

² *Institute of Chemical Sciences, Heriot-Watt University, Edinburgh, EH14 4AS, United Kingdom*

Abstract

Time-resolved photoelectron imaging was used to study non-adiabatic relaxation dynamics in gas-phase indole following photo-excitation at 267 nm and 258 nm. Our data analysis was supported by various *ab initio* calculations using both coupled cluster and density functional methods. The highly differential energy- and angle-resolved information provided by our experimental approach provides extremely subtle details of the complex interactions occurring between several low-lying electronically excited states. In particular, new insight into the role and fate of the mixed Rydberg-valence $3s/\pi\sigma^*$ state is revealed. This includes population residing on the excited state surface at large N-H separations for a relatively long period of time (~ 1 ps) prior to dissociation and/or internal conversion. Our findings may, in part, be rationalized by considering the rapid evolution of this state's electronic character as the N-H stretching coordinate is extended - as extensively demonstrated in the supporting theory. Overall, our findings highlight a number of important general caveats regarding the nature of mixed Rydberg-valence excited states, their spectral signatures and detection sensitivity in photoionization measurements, and the evaluation of their overall importance in mediating electronic relaxation in a wide range of small model-chromophore systems providing bio-molecular analogues – a topic of considerable interest within the chemical dynamics community over the last decade.

^a Present Address: *School of Chemistry, University of Edinburgh, Edinburgh, EH9 3JJ, United Kingdom*

^b E-mail: D.Townsend@hw.ac.uk

I. INTRODUCTION

In a previous publication, hereafter referred to as Paper I,¹ we reported the results of a time-resolved photoelectron spectroscopy (TRPES) study, supported by *ab initio* calculations, investigating the non-adiabatic relaxation dynamics of gas-phase indole and 5-hydroxyindole following ultraviolet (UV) excitation. Indole based chromophores form the basic building block units of the eumelanin pigments that occur frequently in Nature and serve to protect organisms from the potentially damaging effects of UV light.²⁻⁴ As such, developing a more detailed understanding of the primary photophysics operating in this important class of system is clearly of great potential interest and value.

The work described in Paper I employed excitation wavelengths of 249 nm and 273 nm. In the case of 249 nm excitation, our key findings were that initial excitation in indole was exclusively to a valence state of singlet $\pi\pi^*$ character with subsequent “ultrafast” (<100 fs) internal conversion leading to two parallel decay mechanisms via either a second, lower lying singlet $\pi\pi^*$ state or a state of mixed 3s Rydberg/ $\pi\sigma^*$ valence character that is potentially dissociative along the N-H stretching coordinate. Following the historical notation of Platt,⁵ and consistent with Paper I, the initially excited $\pi\pi^*$ state is denoted 1L_a and the lower lying $\pi\pi^*$ state as 1L_b . Unlike Paper I, however, we shall refer to the mixed Rydberg-valence state as $3s/\pi\sigma^*$ throughout, rather than simply using the label $^1\pi\sigma^*$. This is to reinforce the point that at short N-H distances the 3s Rydberg character dominates, with evolution towards greater σ^* character becoming increasingly important as the N-H bond extends⁶ (a fact that will be of some significance for the discussion of the new findings presented herein). More generally, low-lying excited electronic states formed via Rydberg-valence interactions are now recognised as a common feature in the excited state photochemistry of many molecular systems, including biological chromophores such as indoles, phenols, pyrroles, imidazoles

and purines (including the DNA bases adenine and guanine). Over the last decade, a great deal of theoretical and experimental work has been undertaken in studying the role such states play in mediating electronic relaxation following UV excitation. Although often exhibiting little or no oscillator strength in single photon absorption, of particular interest is the possibility of these states providing a rapid and efficient route for non-adiabatic relaxation back to the electronic S_0 ground state, thereby imparting an inherent “photostability”.⁷ Recent reviews by Ashfold and co-workers⁸ and Roberts and Stavros⁹ provide an excellent overview of this work. A review by Reisler and Krylov also provides an in-depth discussion of the Rydberg-valence interaction.¹⁰

A key additional conclusion reported in Paper I was that, following 273 nm excitation, the same parallel relaxation dynamics seen at 249 nm still appeared to be occurring (i.e. the 1L_a state decaying via *either* the 1L_b or $3s/\pi\sigma^*$ states – although some direct excitation to the lower-lying 1L_b state was also now evident). Of particular interest here was the fact that the $3s/\pi\sigma^*$ state still appeared to participate as an internal conversion pathway for the 1L_a state even though 273 nm excitation is below the energetic threshold for the onset of H-atom elimination via direct dissociation on the $3s/\pi\sigma^*$ potential surface reported by Ashfold and co-workers.¹¹ These authors used H (Rydberg) photofragment translational spectroscopy to establish that this onset lies at 263 nm. These findings illustrate an important example of the complementary nature of different experimental approaches (with different associated observables) because the previously reported appearance of high-kinetic H atom fragments at wavelengths shorter than 263 nm allowed us to attribute spectral features in our TRPES data at 249 nm to the $3s/\pi\sigma^*$ state. The presence of the same spectral features in our 273 nm data then enabled us to infer the $3s/\pi\sigma^*$ state was still playing an active role in the relaxation dynamics below the direct N-H fission threshold – although we were unable to definitively

determine the explicit decay mechanism and therefore the ultimate fate of the $3s/\pi\sigma^*$ state in this instance.

A detailed review of previously reported literature relating to the excited state spectroscopy and dynamics of indole up to mid-2011 may be found in Paper I. The reader is directed to that work for additional background information beyond that already discussed above. Three relevant studies reported since publication of our earlier findings are, however, now briefly highlighted here. Longarte and co-workers have undertaken time-resolved ion-yield measurements exciting indole over a range of UV wavelengths spanning the 283-243 nm region.¹² In general agreement with the findings of Paper I, these authors also suggested parallel decay pathways following excitation to the 1L_a state via either 1L_b or $3s/\pi\sigma^*$, although the latter mechanism was only directly apparent at excitation wavelengths < 263 nm (consistent with the observed N-H fission threshold). Additional evidence in support of the $^1L_a \rightarrow ^1L_b$ internal conversion pathway has also been provided by theoretical studies by Lindh and co-workers.¹³ Finally, very recent TRPES work by Ullrich and co-workers has investigated 200 nm excitation in indole.¹⁴ Here the initially prepared 1B_b electronic state undergoes extremely rapid internal conversion to 1L_a , from where the subsequent dynamics were, once again, interpreted to proceed in parallel via either the 1L_b or $3s/\pi\sigma^*$ states, albeit on slightly faster timescales due to the higher internal energy resulting from the shorter wavelength pump.

Here we report the findings of a new time-resolved photoelectron imaging (TRPEI) study using pump excitation wavelengths of 267 nm and 258 nm. Energetically, this excites indole either slightly above or slightly below the aforementioned 263 nm threshold for $3s/\pi\sigma^*$ mediated H atom dissociation. The additional information afforded by the angle-resolved imaging data (something not available in our earlier, angle-integrated TRPES measurements)

reveals detailed new insight into the dynamical evolution and ultimate fate of the $3s/\pi\sigma^*$ state. This highly-differential approach, along with the detailed insight provided by supporting *ab initio* calculations describing this state's mixed Rydberg-valence character vs. N-H extension, are key factors our reaching our final conclusions. More generally, we also note that several aspects of our findings – particularly in regard to detection sensitivity – may be more broadly applied to direct spectroscopic interrogation of “ $\pi\sigma^*$ ” states in a wide range of molecular systems. This includes many species invoked as bio-molecular analogues of naturally occurring chromophores.

II. EXPERIMENTAL

Our experimental setup has been described in detail elsewhere.¹⁵ Indole (Sigma-Aldrich, 99%) was introduced into the source chamber of a differentially pumped photoelectron spectrometer via a pulsed molecular beam valve.¹⁶ Samples were placed in a small cartridge within the valve body and helium (5 bar) was used as a carrier gas. After travelling through a skimmer ($\varnothing = 1.0$ mm), the molecular beam entered the main interaction chamber and was intersected at 90° by co-propagating UV pump (267 nm or 258 nm) and probe (300 nm) pulses. These were derived from the 800 nm fundamental output of a regeneratively amplified Ti:Sapphire laser system (Spectra-Physics, Spitfire Pro/Empower) seeded by a Ti:Sapphire oscillator (Spectra Physics, Tsunami/Millennia Pro).

The 267 nm pump was the third harmonic generated from one portion of the 800 nm fundamental output using a pair of thin β -barium borate (BBO) crystals. The 258 nm pump was obtained by sum-frequency mixing a separate portion of the 800 nm output with the signal beam from an optical parametric amplifier (Spectra Physics, OPA-800C) in a thin BBO crystal. This produced light in the visible region which was then frequency doubled into the UV using a second BBO crystal. In each case the pump was attenuated to ~ 1.2 $\mu\text{J}/\text{pulse}$ and

material dispersion compensation was achieved using a single-pass calcium fluoride prism compressor. The probe beam (300 nm, $\sim 2.0 \mu\text{J}/\text{pulse}$) was obtained by twice frequency doubling the output of a second optical parametric amplifier (Light Conversion, TOPAS Prime-U). The probe wavelength was chosen to ensure that it would induce no resonant absorption in indole, eliminating unwanted “probe-pump” signals.¹ Dispersion management of this beam line was achieved using a single-pass fused silica prism compressor. Temporal delay between the pump and the probe was precisely incremented using a linear translation stage and controller running under automated PC command. The pump and probe beams were combined on a thin dichroic mirror and focussed into the spectrometer using a 25 cm fused silica lens.

Pump-probe ionisation of the indole sample took place between the electrodes of an electrostatic lens set-up optimised for velocity-map imaging.¹⁷ A 40 mm MCP/P47 phosphor screen detector was used in conjunction with a CCD camera (640×480 pixels) to image the resulting photoelectrons. Systematic length adjustment of the prism compressors in each beam line gave a pump-probe cross correlation of 120 ± 10 , recorded directly inside the spectrometer from non-resonant ($1 + 1'$) multiphoton ionization of pyrrole.¹⁸ This data was also used for energy calibration of the instrument. Indole data collection consisted of scanning the translation stage repeatedly between pump-probe delays of -400 fs to +500 fs in 50 fs increments and +500 fs to +20 ps in a series of 9 exponentially increasing time steps. At each delay setting, photoelectron images of time-invariant one-colour pump alone and probe alone signals were recorded in addition to the pump-probe data (for background subtraction). Prior to commencing photoelectron data collection, the spectrometer was switched to ion detection mode to ensure that only the indole monomer was present in the molecular beam.

III. RESULTS

A. Time-resolved Photoelectron Spectra

Fig. 1 shows representative photoelectron images resulting from (1 + 1') ionisation of indole following 258 nm excitation at selected pump-probe delay times Δt . These data were generated by subtracting one-colour pump-alone and probe-alone background images from the raw pump-probe image. Following application of a rapid matrix inversion approach (described in detail elsewhere¹⁵), time-resolved photoelectron spectra were generated from the full set of background-subtracted image data recorded at both pump wavelengths. These are shown in Fig. 2 (note the mixed linear-logarithmic time axis). In each case the spectra look very similar, displaying a weak, very short-lived feature in the region around 0.8-1.0 eV and a long-lived feature at lower photoelectron kinetic energies.

Time-dependence of the photoelectron data was analysed using a standard Levenberg-Marquardt global fitting routine wherein the 2D data $S(E, \Delta t)$ are expressed as:

$$S(E, \Delta t) = \sum_i A_i(E) \cdot P_i(\Delta t) \otimes g(\Delta t) \quad (1)$$

Here $A_i(E)$ is the decay associated spectrum (DAS) of the i^{th} data channel, which has a time dependent population $P_i(\Delta t)$ described by a series of exponentially decaying functions (all of which are set to originate from $\Delta t = 0$) and $g(\Delta t)$ is the experimentally determined Gaussian cross-correlation function. This approach gives the relative amplitude of each exponential component as a function of photoelectron kinetic energy.¹⁹ As in Paper I, satisfactory fits to the time-resolved photoelectron data required three exponentially decaying functions. These exhibited time constants of $\tau_1 = 120 \pm 10$ fs and $\tau_2 = 1.0 \pm 0.1$ ps (267 nm) or $\tau_1 = 120 \pm 10$ fs and $\tau_2 = 0.9 \pm 0.1$ ps (258 nm). For both pump wavelengths the third time constant τ_3 was extremely long, effectively describing a step function over the range of pump-probe delays sampled. To illustrate the good quality of this model, the fit to the 258 nm data and the associated residual are also included in Fig. 2.

Fig. 3 shows the fitted DAS plots associated with each of the three time constants for both excitation wavelengths. Maximum $(1 + 1')$ photoelectron kinetic energy cut-offs are also indicated, calculated on the basis of the pump (267 nm/4.64 eV or 258 nm/4.81 eV) and probe (300 nm/4.13 eV) energies along with the $D_0 (\pi^{-1})$ adiabatic ionisation potential (7.76 eV).²⁰⁻²³ Particular features of note in Fig. 3 are: (i) for both 267 nm and 258 nm excitation, the maximum in the τ_1 DAS sits at ~ 0.8 eV (as also previously observed for 273 nm and 249 nm excitation) and no progression extends up to the maximum energy cut-off. This suggests (i) a reasonably strong propensity for diagonal ionisation from the initially prepared excited state (an expanded discussion may be found Paper I); (ii) the τ_1 DAS at both excitation wavelengths show significant negative amplitude at kinetic energies < 0.6 eV, providing a strong indication of sequential dynamics and (iii) the τ_2 DAS exhibit essentially zero amplitude in the kinetic energy region below 0.3 eV.

B. Photoelectron Angular Distributions

For $(1+1')$ ionization using parallel linear polarizations, the time-dependence of the photoelectron angular distributions (PADs) obtained may be expressed as a function of the electron kinetic energy E and the pump-probe delay time Δt in terms of the anisotropy parameters β_2 and β_4 :^{24, 25}

$$I(E, \Delta t, \theta) = \frac{\sigma(E, \Delta t)}{4\pi} \left[1 + \beta_2(E, \Delta t)P_2(\cos \theta) + \beta_4(E, \Delta t)P_4(\cos \theta) \right] \quad (2)$$

Here the $P_n(\cos \theta)$ terms are the n^{th} -order Legendre polynomials, $\sigma(E, \Delta t)$ is the time-dependent electron energy distribution and $\theta = 180^\circ$ is defined by a vertical line running fully through the images shown in Fig. 1 via the centre point. Fitting to our data using Eq. 2 reveals that, within statistical uncertainty, β_4 is effectively zero over all regions of the time-dependent photoelectron spectra recorded at both 267 nm and 258 nm excitation. However, the PADs do

exhibit some variation in β_2 as a function of time, energy and pump wavelength. This is illustrated in Fig. 4(a-c), which plots the temporal evolution of β_2 averaged over the 0.05-0.30 eV, 0.30-0.70 eV and 0.70-0.95 eV regions. Within each of these three energy partitions temporal trends in the data are consistent. Between 0.05-0.30 eV β_2 evolves rapidly towards higher values before reaching a plateau. Rising exponential fits to this data yield time constants of 140 ± 30 fs (258 nm) and 90 ± 30 fs (267 nm) – comparable to the τ_1 decay values obtained in the corresponding DAS fits. In the high energy region (0.70-0.95 eV) β_2 exhibits a rapid decrease, with exponential decay constants of 120 ± 40 fs (258 nm) and 140 ± 50 fs (267 nm). In the 0.30-0.70 eV region, the evolution of β_2 is more complex. At small Δt values the general behaviour and timescales of the rapid decay appear very similar to the equivalent feature in the 0.70-0.95 eV region. At longer pump-probe delays, however, β_2 now undergoes a subsequent increase. The overlapping rising and decaying signals in this region do not permit reliable extraction of a numerical time constant for this evolution, but β_2 reaches a plateau in ~ 1 ps – considerably longer than the rise seen in the 0.05-0.30 eV region and broadly comparable to the τ_2 timescales obtained in the DAS fits. Finally, Fig. 4(d) shows a plot of β_2 vs. photoelectron kinetic energy for 258 nm excitation at zero pump-probe delay, superimposed on the corresponding photoelectron spectrum. Right up to the high-energy signal cut-off β_2 is relatively small (< 0.45), with no strong anisotropy evident over the entire spectral range. Similar observations are also made in the equivalent 267 nm data.

IV. THEORY

A. State Properties vs. N-H Extension

Paper I presented extensive *ab initio* calculations on indole, performed using several different theoretical approaches. This output included excited state energies and oscillator strengths, excited state orbital visualizations, potential energy cuts along the N-H stretching

coordinate and branching space vector plots for various conical intersections. Here we have further expanded our theoretical investigations by evaluating the evolution of several additional physical properties of indole as a function of N-H bond extension. We have previously reported a similar undertaking for aniline, where such data proved extremely instructive in interpreting certain aspects of experimental TRPEI measurements.⁶ Our computational approach employed linear response coupled cluster (LR-CC) theory (aug-cc-pVDZ basis), with the exponential cluster expansion truncated at singles and doubles, i.e., LR-CCSD. In our previous work we showed that connected triples have only a very small (~ 0.1 eV) effect on vertical electronic excitation energies. We have further used equation of motion coupled cluster theory, again truncated at single and doubles (EOM-CCSD), to analyse the character of the excited states at each geometry. It is worthwhile noting that EOM-CCSD and LR-CCSD formally give an identical excitation spectrum, although transition properties are slightly theoretically improved with LR-CCSD. Initial density functional theory optimization (B3LYP/aug-cc-pVDZ) was performed for the indole ground state geometry using Gaussian09.²⁶ All excited state property calculations described in this section were performed using Dalton2015.^{27,28}

Fig 5(a) plots the normalized EOM-CCSD right eigenvector amplitudes for the orbital transition relating to the $3s/\pi\sigma^*$ contribution to the overall mixed Rydberg-valence state (to which $3s/\pi\sigma^*$ is the dominant contributor - hence the shorthand state label - but there are additional smaller contributions from numerous other states as well). This falls from 0.62 at 1.01 Å to 0.36 at 1.4 Å and beyond. Fig 5(b) shows the corresponding evolution of the (un-normalized) LCAO coefficient magnitude for the un-contracted nitrogen 3s basis function *within* the $3s/\pi\sigma^*$ state (not the Rydberg-valence state overall). This drops by a factor of ~ 2.5 over the same region. Taken together, these data clearly reveal a significant reduction of 3s character (at the expense of more valence character) in the excited Rydberg-valence state as

the N-H bond is extended. Such behavior is very similar to that seen previously in aniline⁶ and, more generally, is likely to be common to many species exhibiting similar mixed Rydberg-valence states.

As discussed previously by Reisler and Kryov,¹⁰ a useful property for parameterizing excited state Rydberg character is the size of the isotropic invariant of the second-moment electronic charge distribution tensor relative to the S_0 ground state $\Delta \langle r_{iso}^2 \rangle$. For a given electronic state $\langle r_{iso}^2 \rangle$ is obtained from the average of the trace of the second moment tensor, i.e., $\langle r_{iso}^2 \rangle = \frac{1}{3}(\langle x^2 \rangle + \langle y^2 \rangle + \langle z^2 \rangle)$. Valence states typically exhibit $\Delta \langle r_{iso}^2 \rangle$ values close to 1 \AA^2 , whereas for 3s Rydberg states this value is an order of magnitude larger. The evolution of $\Delta \langle r_{iso}^2 \rangle$ vs. N-H bond extension for the 1L_a , 1L_b and $3s/\pi\sigma^*$ states is shown in Fig. 5(c). For the two excited states of $\pi\pi^*$ character $\Delta \langle r_{iso}^2 \rangle$ is small ($< 1.5 \text{ \AA}^2$) at all geometries. In contrast, for the $3s/\pi\sigma^*$ state $\Delta \langle r_{iso}^2 \rangle$ decreases considerably as the N-H bond is extended, falling from 15.5 \AA^2 to 4.1 \AA^2 over the range of distances sampled. Once again, this is consistent with our previous observations in aniline and serves to illustrate the rapid and dramatic reduction in the Rydberg character of this state as the N-H bond extends. One key implication of this evolution is that single-photon ionization from the vertical Franck-Condon (FC) region (where the 3s Rydberg character is large) would, at a simple “atomic” level of approximation, give rise to photoelectron partial waves of predominantly p character, peaking along the laser polarization axis and exhibiting a β_2 close to the limiting value of 2. Furthermore, the Rydberg character of the state should also give rise to a strong propensity for diagonal ionization, producing a narrow peak in the photoelectron spectrum. These effects potentially provide a distinct and extremely useful signature of the $3s/\pi\sigma^*$ state and are nicely illustrated in, for example, ionization from the S_2

state of aniline.^{6, 29} In contrast, once the N-H bond is extended these characteristic ionization signatures may not be readily observed as the 3s Rydberg character is significantly reduced and σ^* valence character now dominates. Definitive assignment of the 3s/ $\pi\sigma^*$ state in this situation (i.e. as may occur if the state is only populated indirectly via non-adiabatic decay) is therefore likely to be a more challenging undertaking.

Finally, the isotropic polarizability volume ($\bar{\alpha}$) was also investigated for all electronic states of relevance to this study. This is related to the trace of the electronic polarizability tensor, i.e., $\bar{\alpha} = \frac{1}{3}(\alpha_{xx} + \alpha_{yy} + \alpha_{zz})$. As seen in Fig. 5(d), the 3s/ $\pi\sigma^*$ state polarizability volume decreases rapidly with increased N-H distance, being 110 Å³ at 1.01 Å and falling to below 5 Å³ at 1.50 Å. Values obtained for the ¹L_a, ¹L_b and S₀ states remain broadly consistent across all N-H extensions although it is interesting to note that $\bar{\alpha}$ (¹L_b) is considerably smaller (~3 Å³) than that obtained for the ¹L_a and S₀ states (~16 Å³).

B. Photoionization Cross-Section vs. Isotropic Polarizability Volume

Time-resolved techniques employing photo-reactant ionization attempt to track population evolving from an initially prepared electronic state (or set of states) towards a final set of photoproduct outcomes. In many cases this may involve multiple non-adiabatic pathways. Significant variations in the relative ionization cross-sections of the various states populated along the reaction coordinate(s) therefore lead to major changes in effective detection sensitivity as the system evolves towards the product asymptote. This is in addition to further competing issues relating to FC factors associated with the ionization event and the effects of any molecular alignment resulting from the pump excitation step. Therefore, although highly differential measurements such as those afforded by TRPEI may reveal extremely subtle and detailed mechanistic information associated with a specific decay pathway, it is often extremely difficult to discuss photoproduct branching ratios (i.e. the

relative importance of one pathway over another) in a manner that is qualitative, let alone quantitative. This issue is further compounded by the fact that, at present, accurate theoretical/computational evaluation of ionization cross-sections for molecules of modest size (i.e. comparable to that of indole) is extremely challenging – particularly for excited states – and has not, to the best of our knowledge, been reliably demonstrated on a consistent basis.

In light of the issues outlined above, it is therefore appealing to try and seek correlations between photoionization cross-sections and specific physical molecular properties that may be evaluated in a relatively straightforward and computationally inexpensive manner. This may ultimately help facilitate at least qualitative discussion of relative branching in non-adiabatic dynamical processes studied using photoreactant ionization. Strong correlations have previously been reported between isotropic electronic polarizability volume and ground state electron impact ionization cross-section, as summarized (and also demonstrated) by Vallance and co-workers.³⁰ This observation has already served as an initial motivation for us to begin exploring similar effects in low-energy photoionization.⁶ Computationally evaluated electronic polarizability volume data for 27 molecular systems^{30, 31} were correlated with experimentally determined ground state photoionization cross-sections obtained from a number of sources.³²⁻⁴⁰ At a photon energy of 11.5 eV, a highly significant relationship between the two quantities was clearly evident – although data for additional systems with relatively large polarizability volumes ($>12 \text{ \AA}^3$) would have been desirable to establish this trend more generally. In order to address this, we have now evaluated isotropic polarizability volume data for 10 new molecules (see Table I) using an identical computational approach to that used previously. The new species were specifically chosen as they exhibit very high experimental photoionization cross-sections ($> 60 \text{ Mb}$ at 11.5 eV) and so large polarizability volumes would be predicted on the basis of the previously suggested trend. Briefly, calculations were performed with Gaussian09²⁶ and

used the PBE0 density functional⁴¹ in conjunction with a basis set denoted Sadlej (H+d). This is a modified form of the Sadlej triple- ζ basis set⁴² (originally developed specifically for polarizability calculations) where additional un-contracted d orbitals with exponent $\zeta = 0.1$ have been added to each hydrogen atom. A more detailed description of this approach and a comprehensive evaluation of its excellent performance with respect to other, computationally more expensive strategies may be found in Ref. 30. Our new data is presented in Table I. Several previously reported results from Vallance and co-workers were also successfully reproduced in order to validate that our application was fully consistent.

Fig. 6 plots calculated isotropic polarizability volume vs. experimentally determined cross-section for ground state photoionization of all 37 molecular systems at 11.5 eV. A linear fit to this data produces a correlation coefficient of $r = 0.93$ – a highly significant correlation and slightly better than that obtained previously with the more limited data set of 27 species.⁶ At lower photoionization energies, the same trend is also evident. Photoionization cross-section data 10.5 eV and 9.5 eV yield correlation coefficients of $r = 0.78$ and 0.80 , respectively. Although these values are slightly reduced relative to 11.5 eV, the sample sizes are still sufficiently large (32 and 18 molecules) to suggest that a highly significant correlation persists as the photon energy is reduced (the sample size decreases as the photon energy no longer exceeds the ionization potential for some of the systems under consideration). The data in Fig. 6 reinforces the strong link we have suggested previously between increasing polarizability volume and larger (low-energy) photoionization cross section. We stress, however, that a great deal of additional work is required to establish if the observed trend extends consistently in the same manner to even higher values of the polarizability volume, applies equivalently to electronically excited states and also persists at further reduced ionizing photon energies (as often used in two-colour pump-probe measurements). Nevertheless, we feel that our initial findings offer some interesting insights and hope they

will serve as a stimulus for future work in this area. The nature of the clear correlations we observe may perhaps be rationalized by the fact that both the ionization cross section and the isotropic polarizability volume have a similar mathematical dependence on the electronic dipole matrix.⁴³ More subtly, however, the electronic dipole matrix elements for $\bar{\alpha}$ involve the initial ground state wavefunction, the electric dipole operator and an excited state wavefunction. A sum is then made over all excited states to evaluate the polarizability volume. On the other hand, the electronic dipole matrix elements associated with the ionization cross-section incorporate the initial ground state wavefunction, the electric dipole operator and the final (ion + free electron) state wavefunction. The photon energy dependent nature of the interaction between the outgoing free electron and the ionic core leads to the molecular photoionization cross-section evolving rapidly in the region just above the ionization onset and exhibiting a maximum which is typically observed at 20-30 eV photon energy.⁴⁴ In spite of these differing factors, it will be interesting in future to see if the polarizability volume can provide an heuristic tool with some generality for (at least) qualitative discussion of population evolution dynamics in time-resolved ionization experiments using low-energy UV probes.

Within the context of the work presented here, our polarizability vs. cross-section data are of considerable significance as the data presented earlier in Fig. 5(d) clearly show an extremely large (i.e. order of magnitude or more) difference in the polarizability volumes for the ${}^1L_a/{}^1L_b$ states vs. the $3s/\pi\sigma^*$ state at short N-H distances. Initially removing FC and excited-state alignment effects from the argument, we therefore (conservatively) suggest that the $3s/\pi\sigma^*$ ionization cross-section is at least an order of magnitude larger than that of the ${}^1L_a/{}^1L_b$ states at the ground state geometry. This implies that if the $3s/\pi\sigma^*$ state is directly excited in the FC region – even very weakly – we would expect to have extremely high sensitivity to detecting it in TRPEI measurements. Such an effect is clearly evident in our

previous work on aniline and its methyl-substituted derivatives.⁶ However, as the N-H bond extends (and $\bar{\alpha}$ decreases), this detection sensitivity will reduce rapidly – particularly as FC factors for ionization are then also likely to become more unfavourable at the extended N-H geometry. In cases where the $3s/\pi\sigma^*$ state is only populated via non-adiabatic coupling (for which an extended N-H bond is a pre-requisite¹) the sensitivity to its detection using ionization is likely to be reduced greatly, becoming similar to, or even smaller than the ${}^1L_a/{}^1L_b$ states.

V. DISCUSSION

The DAS plots shown in Fig. 3 for pump wavelengths of 267 nm and 258 nm are in good overall agreement with those previously reported at 273 nm and 249 nm in Paper I. The decay lifetimes, shapes and positions of features in the spectra associated with each of the three time constants required to accurately fit the data are similar in all cases. Any small differences in relative peak amplitudes are due to an energy-dependent transmission efficiency of the magnetic bottle spectrometer used in our earlier study. As noted previously, the τ_1 DAS exhibits significant negative amplitude below 0.6 eV. Since all three exponentially decaying functions used in the fit to the raw photoelectron spectra originate from zero pump-probe delay, this provides a clear indication of the system undergoing sequential dynamics – negative amplitude associated with the τ_1 DAS in this low energy region is effectively compensating for positive amplitude at short delay times associated with a longer-lived sequential feature (i.e., one not truly originating from $\Delta t = 0$) described by a different DAS in the same energy region. As argued in detail in Paper I, we assign the positive amplitude component of the τ_1 DAS in the region > 0.6 eV to direct excitation to the 1L_a state. We also attribute the negative amplitude τ_1 DAS features to non-adiabatic population transfer between the 1L_a and 1L_b states. Such a mechanism is strongly supported by our own previous

theoretical studies and also those of others.^{1, 13, 45} The τ_3 DAS describing the very long-lived features in the photoelectron data is then attributable to the 1L_b state. Since the negative τ_1 DAS amplitude does not fully “mirror” the positive amplitude present in the τ_3 DAS, we may also infer that some of the τ_3 signal originates from zero pump-probe delay. This implies that, in addition to population via the 1L_a state, there must also be some direct 1L_b excitation. At 267 nm the extent of this direct transition to the long-lived state appears more significant than at 258 nm – as might be reasonably expected on the basis of absorption band decomposition studies performed on indole embedded in solid matrices.^{46, 47}

Additional support for the $^1L_a/^1L_b$ electronic coupling interaction comes from the PAD data: In previous work investigating non-adiabatic dynamics in a range of molecular systems we, and others, have argued that the temporal evolution of the PAD provides a sensitive signature of the evolution of excited state electronic character.^{6, 15, 48-50} The DAS plots in Fig. 3 clearly show that in the region between 0.05-0.30 eV the τ_2 spectrum exhibits zero amplitude. As such, temporal changes in the photoelectron anisotropy parameter β_2 within the 0.05-0.30 eV region should reflect evolution of the electronic character of the 1L_b state exclusively. As evident from Fig. 4(a), β_2 is clearly seen to evolve rapidly to larger values in this region following excitation at both 267 nm and 258 nm. Fitted exponential rise times associated with this process (~100 fs) are also very well-matched to the decay times for β_2 between 0.70-95 eV (Fig. 4(c)). Here the only significant DAS amplitude is in the τ_1 component (see Fig. 3), which is attributed to the 1L_a state. The complementary rise and fall of the photoelectron anisotropy in these two distinct energy regions therefore gives rise to a strong signature of the ultrafast non-adiabatic coupling between the two $\pi\pi^*$ states.

The τ_2 lifetimes of 1.0 ps (267 nm) and 0.9 ps (258 nm) show an energetic trend (see Fig. 7) that is consistent with values reported in Paper I following 273 nm and 249 nm

excitation (1.2 ps and 0.7 ps, respectively). Previously, we assigned the τ_2 DAS to decay of the $3s/\pi\sigma^*$ state following <100 fs population from 1L_a (i.e. a process competing in parallel with decay via the 1L_b state). Pump wavelengths used in this present study were specifically chosen to excite indole slightly below or slightly above the experimentally determined threshold for direct N-H bond fission on the $3s/\pi\sigma^*$ potential surface (263 nm). Following 258 nm excitation at least some fraction of the $3s/\pi\sigma^*$ state population therefore rapidly dissociates directly along the N-H stretching co-ordinate. Following 267 nm excitation, however, this pathway would seem to be inaccessible. In Paper I we speculated that (for the case of 273 nm excitation) this was due to there being insufficient energy to directly overcome a small (~ 0.45 eV) barrier predicted to lie along the N-H coordinate of the $3s/\pi\sigma^*$ potential surface and that another decay pathway was operating instead.^{1, 29} However, our attempts to locate a conical intersection involving the $3s/\pi\sigma^*$ state at constrained N-H bond distances proved unsuccessful. From Fig. 7 it is clear that as the excitation wavelength is shortened from 273 nm to 249 nm there is a gradually decreasing trend in lifetime that would seem to be inconsistent with a shift from (just) below a potential barrier to a fully open channel. In addition, $3s/\pi\sigma^*$ population being trapped (or even initially prepared) at short N-H distances as the dominant $3s$ character of the state in this region (see Fig. 5) would clearly manifest in some region of the observed PAD – i.e. a strong, energetically narrow photoelectron peak exhibiting high positive β_2 anisotropy (such as that seen in aniline⁶). The fact that such a feature is not present at either pump wavelength leads us to reaffirm that the $3s/\pi\sigma^*$ state is only populated indirectly via non-adiabatic processes and conclude that previous estimates of the barrier along the N-H stretching coordinate appear to be too high.

In light of the above conclusion, it seems that the wavelength-dependent propensity for direct N-H bond fission must therefore be mediated by the rate at which the conical

intersection connecting the $3s/\pi\sigma^*$ and S_0 states is traversed. This conical intersection occurs at highly extended N-H distances (>1.8 Å) and is well established theoretically.^{1, 7, 51, 52} Slower wavepacket motion through this region (corresponding to longer excitation wavelengths) would be expected to give rise to enhanced non-adiabatic behaviour (i.e. increased population transfer to S_0 rather than direct N-H fission). However, this simple picture is difficult to reconcile with the fact that our τ_2 lifetimes (~ 1 ps) are extremely long in the context of an N-H stretching vibration. Others have also observed “long” $3s/\pi\sigma^*$ decay lifetimes and, very recently, seen extremely similar extended timescales for the concomitant H atom elimination in indole following excitation in the 250-260 nm region.^{12, 53} However, this is consistent with the previous observation of *isotropic* H atom recoil from dissociation on the $3s/\pi\sigma^*$ potential¹¹. This clear lifetime anomaly leads us to consider the possibility that the τ_2 DAS is therefore not a signature of the $3s/\pi\sigma^*$ state, but rather a consequence of ultrafast intramolecular vibrational redistribution (IVR) within the 1L_b state (with any $3s/\pi\sigma^*$ spectral signatures being too weak to see in our data). Sub-picosecond IVR processes have previously been reported in several aromatic systems^{6, 15, 29, 54, 55} and in the present experiments we are > 2150 cm^{-1} above the 1L_b origin⁵⁶ – considerably higher than experimentally determined IVR thresholds reported in other aromatic systems.^{57, 58} However, we have seen no evidence in our previous work that ultrafast IVR processes directly lead to any significant PAD evolution.^{6, 15, 29, 59} The ~ 1 ps rise exhibited by β_2 between 0.30-7.0 eV (see Fig. 4(b)) is therefore unlikely to originate from an IVR effect and instead may be attributed to the $3s/\pi\sigma^*$ state decaying and making a reduced contribution to the overall PAD in this energy region. We may then be confident that the τ_2 DAS – which describes behaviour on a similar timescale – must be a signature of the $3s/\pi\sigma^*$ state at both pump wavelengths. We also note that rapid IVR processes occurring on the 1L_b surface might reasonably be

expected to manifest as temporally evolving signatures over the entire 0.05-0.70 eV region. The fact that we see no picosecond evolution of β_2 between 0.05-0.30 eV provides additional evidence to support the $3s/\pi\sigma^*$ interpretation. The lack of a picosecond component in this region also rules out internal conversion between the $3s/\pi\sigma^*$ and 1L_b states as a possible alternative decay pathway.

Finally, the considerable weight of experimental and theoretical evidence presented up to now leads us to the following conclusion for the ultimate fate of the $3s/\pi\sigma^*$ state of indole: Population is prepared non-adiabatically via the optically prepared 1L_a state at extended N-H bond extension (i.e. away from the FC region). At this point the molecule may either undergo N-H bond fission (258 nm) and/or internal conversion to S_0 (258 & 267 nm). Prior to either process occurring, however, population appears to reside on the $3s/\pi\sigma^*$ state surface for a relatively long period of time (~ 1 ps), seemingly restricted to large N-H distances while “encircling” the upper cone of the conical intersection formed between the $3s/\pi\sigma^*$ and S_0 states. A very similar phenomenon has previously been invoked in the \tilde{A} state dissociation of ammonia^{60, 61} and analogies have been drawn with the novel “roaming” mechanism first reported over a decade ago.⁶²⁻⁶⁴ The same idea has also been suggested to explain aspects of the excited state dynamics seen in thioanisole,⁶⁵ methylamine⁶⁶ and aniline.^{67, 68} In the absence of extensive multi-state dynamics simulations and also specifically targeted experimental measurements, the exact details of this process remain an open question for now. However, on the basis of the detection sensitivity arguments outlined earlier, the small polarizability volume and unfavourable FC factors for ionization of the $3s/\pi\sigma^*$ state at extended N-H geometries mean that, even though the τ_2 DAS amplitude is relatively small, our findings offer strong evidence that this pathway may play a significant, and possibly even a dominant role in the overall relaxation dynamics of indole following UV absorption.

VI. CONCLUSION

Time-resolved photoelectron imaging, supported by various *ab initio* calculations, was used to investigate non-adiabatic relaxation in gas-phase indole following excitation at 267 nm and 258 nm. Our data clearly reveal detailed new dynamical insight and this serves as a good illustration of the considerable advantages provided by the highly differential energy- and angle-resolved experimental methodology. The decay of the initially prepared 1L_a state occurs in ~ 100 fs via two parallel competing mechanisms: non-adiabatic coupling to either the long-lived 1L_b state or the $3s/\pi\sigma^*$ state, which exhibits a subsequent decay lifetime of ~ 1 ps. Both pathways appear to be energetically accessible following excitation at both 258 nm and 267 nm and, surprisingly, appear to involve population residing on the $3s/\pi\sigma^*$ state surface at large N-H separations for a relatively long time period (~ 1 ps) prior to dissociation and/or internal conversion. Our findings are also, in part, supported by our calculations tracking the rapid and dramatic evolution of the mixed Rydberg-valence character within the $3s/\pi\sigma^*$ state as the N-H stretching coordinate is extended. This ultimately leads to some important and generalized caveats regarding the spectroscopic detection of such mixed Rydberg-valence states in a wide range of molecular systems. In particular, their assignment in dynamical studies and determining of their overall importance in mediating electronic relaxation in a wide range of small “model-chromophore” systems must be considered with great care – particularly when less differential experimental approaches than TRPEI are employed. Finally, we have further expanded upon some general heuristic observations correlating polarizability volume and low-energy photoionization cross-section. This has relevant implications for tracking sensitivity in experiments employing photoionization to investigate non-adiabatic processes evolving across multiple electronic states, potentially providing a useful heuristic aid for qualitative discussion of branching ratios when analysing/interpreting data obtained from a wide range of systems. We stress, however, that considerably more work

in this area is required to fully establish the general nature of any polarizability volume/photoionization cross-section relationship.

ACKNOWLEDGEMENTS

M.J.P. is supported by the European Research Council under the European Union's Seventh Framework Programme (FP7/2007-2013)/ERC Grant No. 258990. M.M.Z. and J.O.F.T. thank Heriot-Watt University for Ph.D. funding. We also thank S. Ullrich (University of Georgia) and A. Stolow (University of Ottawa) for helpful discussions.

REFERENCES

1. R. Livingstone, O. Schalk, A. E. Boguslavskiy, G. Wu, L. T. Bergendahl, A. Stolow, M. J. Paterson and D. Townsend, *J. Chem. Phys.*, 2011, **135**, 194307.
2. P. Meredith and T. Sarna, *Pigments Cell Res.*, 2006, **19**, 572.
3. P. Meredith, B. J. Powell, J. Reisz, S. P. Nighswander-Rempel, M. R. Pederson and E. G. Moore, *Soft Matter*, 2006, **2**, 37.
4. A. Huijser, A. Pezzella and V. Sundström, *Phys. Chem. Chem. Phys.*, 2011, **13**, 9119.
5. J. R. Platt, *J. Chem. Phys.*, 1949, **17**, 484.
6. J. O. F. Thompson, L. Saalbach, S. W. Crane, M. J. Paterson and D. Townsend, *J. Chem. Phys.*, 2015, **142**, 114309.
7. A. L. Sobolewski, W. Domcke, C. Dedonder-Lardeux and C. Jouvet, *Phys. Chem. Chem. Phys.*, 2002, **4**, 1093.
8. M. N. R. Ashfold, G. A. King, D. Murdock, M. G. D. Nix, T. A. A. Oliver and A. G. Sage, *Phys. Chem. Chem. Phys.*, 2010, **12**, 1218.
9. G. M. Roberts and V. G. Stavros, *Chem. Sci.*, 2014, **5**, 1698.
10. H. Reisler and A. I. Krylov, *Int. Rev. Phys. Chem.*, 2009, **28**, 267.
11. M. G. D. Nix, A. L. Devine, B. Cronin and M. N. R. Ashfold, *Phys. Chem. Chem. Phys.*, 2006, **8**, 2610.
12. R. Montero, A. P. Conde, V. Ovejas, F. Castaño and A. Longarte, *J. Phys. Chem. A*, 2011, **116**, 2698.
13. A. Giussani, M. Merchán, D. Roca-Sanjuán and R. Lindh, *J. Chem. Theory Comput.*, 2011, **7**, 4088.
14. T. J. Godfrey, H. Yu and S. Ullrich, *J. Chem. Phys.*, 2014, **141**, 044314.
15. R. A. Livingstone, J. O. F. Thompson, M. Iljina, R. J. Donaldson, B. J. Sussman, M. J. Paterson and D. Townsend, *J. Chem. Phys.*, 2012, **137**, 184304.
16. U. Even, J. Jortner, D. Noy, N. Lavie and C. Cossart-Magos, *J. Chem. Phys.*, 2000, **112**, 8068.
17. A. T. J. B. Eppink and D. H. Parker, *Rev. Sci. Instrum.*, 1997, **68**, 3477.
18. R. Montero, V. Ovejas, M. Fernández-Fernández, A. Peralta-Conde and A. Longarte, *J. Chem. Phys.*, 2014, **141**, 014303.
19. O. Schalk, A. E. Boguslavskiy and A. Stolow, *J. Phys. Chem. A*, 2010, **114**, 4058.
20. J. Hager, M. Ivanco, M. A. Smith and S. C. Wallace, *Chem. Phys. Lett.*, 1985, **113**, 503.
21. T. Vondrák, S. Sato and K. Kimura, *J. Phys. Chem. A*, 1997, **101**, 2384.
22. J. E. Braun, T. L. Grebner and H. J. Nuesser, *J. Phys. Chem. A*, 1998, **102**, 3273.
23. M. de Groot, J. Broos and W. J. Buma, *J. Chem. Phys.*, 2007, **126**, 204312.
24. K. L. Reid, *Annu. Rev. Phys. Chem.*, 2003, **54**, 397.
25. T. Suzuki, *Annu. Rev. Phys. Chem.*, 2006, **57**, 555.
26. M. J. Frisch, G. W. Trucks, H. B. Schlegel, G. E. Scuseria, M. A. Robb, J. R. Cheeseman, G. Scalmani, V. Barone, B. Mennucci, G. A. Petersson, H. Nakatsuji, M. Caricato, X. Li, H. P. Hratchian, A. F. Izmaylov, J. Bloino, G. Zheng, J. L. Sonnenberg, M. Hada, M. Ehara, K. Toyota, R. Fukuda, J. Hasegawa, M. Ishida, T. Nakajima, Y. Honda, O. Kitao, H. Nakai, T. Vreven, J. A. Montgomery, Jr., J. E. Peralta, F. Ogliaro, M. Bearpark, J. J. Heyd, E. Brothers, K. N. Kudin, V. N. Staroverov, R. Kobayashi, J. Normand, K. Raghavachari, A. Rendell, J. C. Burant, S. S. Iyengar, J. Tomasi, M. Cossi, N. Rega, J. M. Millam, M. Klene, J. E. Knox, J. B. Cross, V. Bakken, C. Adamo, J. Jaramillo, R. Gomperts, R. E. Stratmann, O. Yazyev, A. J. Austin, R. Cammi, C. Pomelli, J. W. Ochterski, R. L. Martin, K. Morokuma, V.

- G. Zakrzewski, G. A. Voth, P. Salvador, J. J. Dannenberg, S. Dapprich, A. D. Daniels, Ö. Farkas, J. B. Foresman, J. V. Ortiz, J. Cioslowski, and D. J. Fox, GAUSSIAN 09, Revision D.01, Gaussian, Inc., Wallingford CT, 2009.
27. K. Aidas, C. Angeli, K. L. Bak, V. Bakken, R. Bast, L. Boman, O. Christiansen, R. Cimraglia, S. Coriani, P. Dahle, E. K. Dalskov, U. Ekström, T. Enevoldsen, J. J. Eriksen, P. Ettenhuber, B. Fernández, L. Ferrighi, H. Fliegl, L. Frediani, K. Hald, A. Halkier, C. Hättig, H. Heiberg, T. Helgaker, A. C. Hennum, H. Hettema, E. Hjertenæs, S. Høst, I.-M. Høyvik, M. F. Iozzi, B. Jansik, H. J. Aa. Jensen, D. Jonsson, P. Jørgensen, J. Kauczor, S. Kirpekar, T. Kjærgaard, W. Klopper, S. Knecht, R. Kobayashi, H. Koch, J. Kongsted, A. Krapp, K. Kristensen, A. Ligabue, O. B. Lutnæs, J. I. Melo, K. V. Mikkelsen, R. H. Myhre, C. Neiss, C. B. Nielsen, P. Norman, J. Olsen, J. M. H. Olsen, A. Osted, M. J. Packer, F. Pawłowski, T. B. Pedersen, P. F. Provasi, S. Reine, Z. Rinkevicius, T. A. Ruden, K. Ruud, V. Rybkin, P. Salek, C. C. M. Samson, A. S. d. Merás, T. Saue, S. P. A. Sauer, B. Schimmelpfennig, K. Sneskov, A. H. Steindal, K. O. Sylvester-Hvid, P. R. Taylor, A. M. Teale, E. I. Tellgren, D. P. Tew, A. J. Thorvaldsen, L. Thøgersen, O. Vahtras, M. A. Watson, D. J. D. Wilson, M. Ziolkowski and H. Ågren, *WIREs Comput. Mol. Sci.*, 2014, **4**, 269.
 28. Dalton, a molecular electronic structure program, Release Dalton2015.0 (2015), see <http://daltonprogram.org>.
 29. J. O. F. Thompson, R. A. Livingstone and D. Townsend, *J. Chem. Phys.*, 2013, **139**, 034316.
 30. J. N. Bull, P. W. Harland and C. Vallance, *J. Phys. Chem. A*, 2012, **116**, 767.
 31. J. N. Bull, J. W. L. Lee and C. Vallance, *Phys. Chem. Chem. Phys.*, 2014, **16**, 10743.
 32. B. Yang, J. Wang, T. A. Cool, N. Hansen, S. Skeen and D. L. Osborn, *Int. J. Mass. Spectrom.*, 2012, **309**, 118.
 33. M. Xie, Z. Zhou, Z. Wang, D. Chen and F. Qi, *Int. J. Mass. Spectrom.*, 2011, **303**, 137.
 34. Z. Zhou, L. Zhang, M. Xie, Z. Wang, D. Chen and F. Qi, *Rapid Commun. Mass Spectrom.*, 2010, **24**, 1335.
 35. M. Xie, Z. Zhou, Z. Wang, D. Chen and F. Qi, *Int. J. Mass. Spectrom.*, 2010, **293**, 28.
 36. J. Wang, B. Yang, T. A. Cool and N. Hansen, *Int. J. Mass. Spectrom.*, 2010, **292**, 14.
 37. Z. Zhou, M. Xie, Z. Wang and F. Qi, *Rapid Commun. Mass Spectrom.*, 2009, **23**, 3994.
 38. J. Wang, B. Yang, T. A. Cool, N. Hansen and T. Kasper, *Int. J. Mass. Spectrom.*, 2008, **269**, 210.
 39. T. A. Cool, J. Wang, K. Nakajima, C. A. Taatjes and A. McIlroy, *Int. J. Mass. Spectrom.*, 2005, **247**, 18.
 40. J. A. R. Samson, G. N. Haddad and L. D. Kilcoyne, *J. Chem. Phys.*, 1987, **87**, 6416.
 41. C. Adamo and V. Barone, *J. Chem. Phys.*, 1999, **110**, 6158.
 42. A. J. Sadlej, *Collect. Czech. Chem. Commun.*, 1988, **53**, 1995.
 43. F. W. Lampe, J. L. Franklin and F. H. Field, *J. Am. Chem. Soc.*, 1957, **79**, 6129.
 44. J. W. Rabalais, *Principles of Ultraviolet Photoelectron Spectroscopy*, Wiley, New York, 1977.
 45. C. Brand, J. Küpper, D. W. Pratt, W. L. Meerts, D. Krügler, J. Tatchen and M. Schmitt, *Phys. Chem. Chem. Phys.*, 2010, **12**, 4968.
 46. M. R. Eftink, L. A. Selvidge, P. R. Callis and A. A. Rehms, *J. Phys. Chem.*, 1990, **94**, 3469.
 47. R. L. Rich, Y. Chen, D. Neven, M. Négrerie, F. Gai and J. W. Petrich, *J. Phys. Chem.*, 1993, **97**, 1781.

48. C. Z. Bisgaard, O. J. Clarkin, G. Wu, A. M. D. Lee, O. Gessner, C. C. Hayden and A. Stolow, *Science*, 2009, **323**, 1464.
49. Y.-I. Suzuki, T. Horio, T. Fuji and T. Suzuki, *J. Chem. Phys.*, 2011, **134**, 184313.
50. G. Wu, P. Hockett and A. Stolow, *Phys. Chem. Chem. Phys.*, 2011, **13**, 18447.
51. A. L. Sobolewski and W. Domcke, *Chem. Phys. Lett.*, 1999, **315**, 293.
52. A. L. Sobolewski and W. Domcke, *J. Phys. Chem. A*, 2007, **111**, 11725.
53. S. Ullrich, *Personal communication*.
54. Y.-Z. Liu, C.-C. Qin, S. Zhang, Y.-M. Wang and B. Zhang, *Acta Phys. -Chim. Sin.*, 2011, **27**, 965.
55. R. S. von Benten, Y. Liu and B. Abel, *J. Chem. Phys.*, 2010, **133**, 134306.
56. G. Berden, W. L. Meerts and E. Jalviste, *J. Chem. Phys.*, 1995, **103**, 9596.
57. R. Matsumoto, K. Sakeda, Y. Matsushita, T. Suzuki and T. Ichimura, *J. Mol. Struct.*, 2005, **735**, 153.
58. G. N. Patwari, S. Doraiswamy and S. Wategaonkar, *J. Phys. Chem. A*, 2000, **104**, 8466.
59. S. E. Greenough, M. D. Horbury, J. O. F. Thompson, G. M. Roberts, T. N. V. Karsili, B. Marchetti, D. Townsend and V. G. Stavros, *Phys. Chem. Chem. Phys.*, 2014, **16**, 16187.
60. J. Biesner, L. Schnieder, G. Ahlers, X. Xie, K. H. Welge, M. N. R. Ashfold and R. N. Dixon, *J. Chem. Phys.*, 1989, **91**, 2901.
61. A. S. Chatterley, G. M. Roberts and V. G. Stavros, *J. Chem. Phys.*, 2013, **139**, 034318.
62. D. Townsend, S. A. Lahankar, S. K. Lee, S. D. Chambreau, A. G. Suits, X. Zhang, J. Rheinecker, L. B. Harding and J. M. Bowman, *Science*, 2004, **306**, 1158.
63. A. G. Suits, *Acc. Chem. Res.*, 2008, **41**, 873.
64. J. D. Rodríguez, M. G. González, L. Rubio-Lago and L. Bañares, *Phys. Chem. Chem. Phys.*, 2014, **16**, 406.
65. J. S. Lim and S. K. Kim, *Nat. Chem.*, 2010, **2**, 627.
66. D.-S. Ahn, J. Lee, J.-M. Choi, K.-S. Lee, S. J. Baek, K. Lee, K.-K. Baek and S. K. Kim, *J. Chem. Phys.*, 2008, **128**, 224305.
67. R. Spesyvtsev, O. M. Kirkby, M. Vacher and H. H. Fielding, *Phys. Chem. Chem. Phys.*, 2012, **14**, 9942.
68. R. Spesyvtsev, O. M. Kirkby and H. H. Fielding, *Faraday Discuss.*, 2012, **157**, 165.

TABLE CAPTIONS

Table I: Isotropic electronic polarizability volume ($\bar{\alpha}$) for several molecules evaluated using the PBE0/Sadlej(H+d) approach. For further details see main text.

Table I

	$\bar{\alpha}$ (\AA^3)
1-Methylnaphthalene	19.72
1,3,5-Trimethylbenzene	16.35
<i>n</i> -Propylbenzene	16.09
Indane	15.25
Styrene	14.84
Phenylacetylene	14.36
<i>n</i> -Methylaniline	14.20
Benzylamine	13.68
Heptane	13.56
Benzonitrile	12.86

FIGURE CAPTIONS

Figure 1: $(1 + 1')$ photoelectron images at selected pump-probe time delays Δt following indole excitation at 258 nm and ionization at 300 nm. Pump-alone and probe-alone signals have been subtracted and the images are 4-fold symmetrised. The right-hand half of the 20 ps image shows the result following application of the matrix inversion method described in Ref. 15. The linear polarization direction of both the pump and probe beams is vertical with respect to the images.

Figure 2: Time-dependent photoelectron spectra of indole obtained following excitation at 267 nm and 258 nm (with subsequent ionization using a 300 nm probe). The data is partitioned into 0.05 eV energy bins. Also shown are the fit to the 258 nm data obtained using the procedure described in the main text along with the associated residuals (i.e. the fit subtracted from the raw data). Time axes are linear to +500 fs and logarithmic between +500 fs and +20 ps. The vertical intensity axes are linear and normalized with respect to the most intense point in each data set.

Figure 3: Decay associated spectra (DAS) obtained from a global exponential fit to the data presented in Fig. 2. For additional details see the main text. The (1σ) uncertainty in the values of τ_1 and τ_2 are ± 10 fs and ± 0.1 ps, respectively. The data is partitioned into 0.05 eV bins and the vertical arrows denote the predicted maximum photoelectron kinetic energy cut-offs.

Figure 4: (a)-(c) Anisotropy parameter β_2 as a function of pump-probe delay averaged over selected photoelectron kinetic energy ranges following indole excitation at 267 nm and 258 nm. Time axes are linear to +500 fs and then logarithmic between +500 fs and +20 ps. Fits were performed over the angular region between $5^\circ \leq \theta \leq 90^\circ$ to eliminate uncertainties from the centre-line noise present in the Abel-inverted images. In (c) the plot is truncated at 250 fs as the signal level in the raw photoelectron data becomes so small that the fit becomes

statistically meaningless. (d) Anisotropy parameter β_2 as a function of photoelectron kinetic energy at zero pump-probe delay (data points) superimposed over the corresponding photoelectron spectrum at zero pump-probe delay (grey line). Error bars represent one standard deviation.

Figure 5: Evolution of electronic state properties for the S_0 (●), 1L_a (✖), 1L_b (□) and $3s/\pi\sigma^*$ (◆) states of indole as a function of N-H bond extension. For additional details, see main text.

(a) Normalized EOM-CCSD right eigenvector amplitude for the $3s/\pi\sigma^*$ state, (b) un-normalized LCAO coefficient of the un-contracted nitrogen 3s basis function within the $3s/\pi\sigma^*$ state, (c) isotropic invariant of the excited-state second-moment of the electronic charge distribution with respect to the ground state, and (d) isotropic electronic polarizability volume. Note that the predicted S_0 equilibrium N-H bond length is 1.02 Å and the $\pi\pi^*$ and $3s/\pi\sigma^*$ states cross at ~ 1.2 Å. For more details see Ref 1.

Figure 6: Ground state photoionization cross-section (at 11.5 eV) vs. isotropic polarizability volume for 37 small molecules. Points labelled (●) use polarizability data from Refs. 30&31 and points denoted (◇) use polarizability data evaluated as part of the present study (see Table I). The experimental cross-section data was taken from Refs 32-40. A linear fit to the data yields a correlation coefficient of $r = 0.93$.

Figure 7: Exponential decay lifetime τ_2 as a function of pump excitation energy. Data labelled (◆) are taken from Ref. 1 and data denoted (◇) are from the present study.

Figure 1

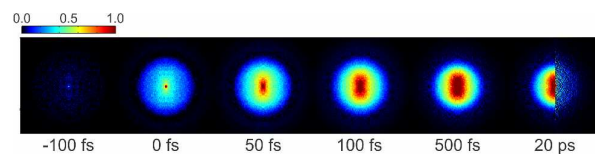


Figure 2

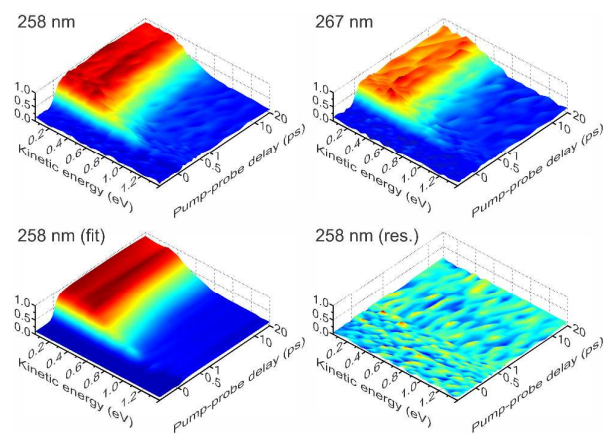


Figure 3

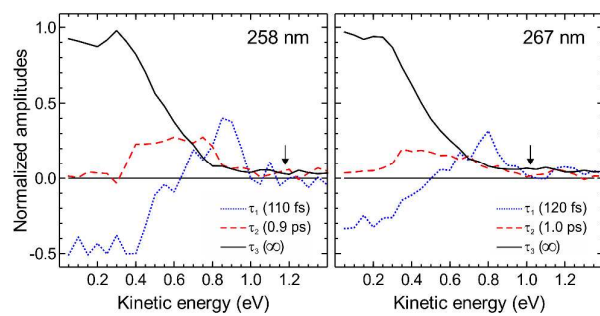


Figure 4

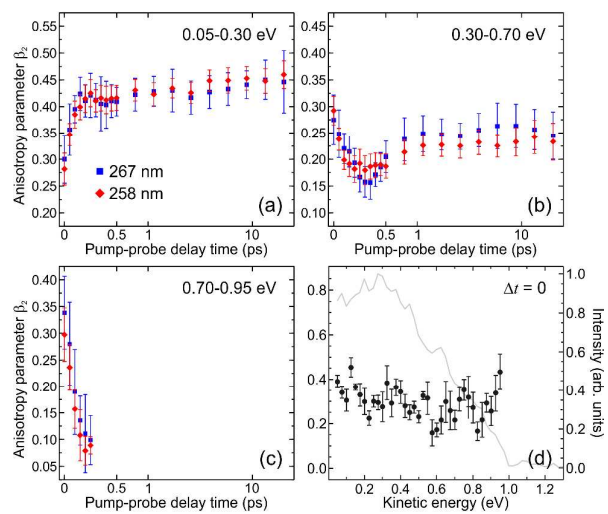


Figure 5

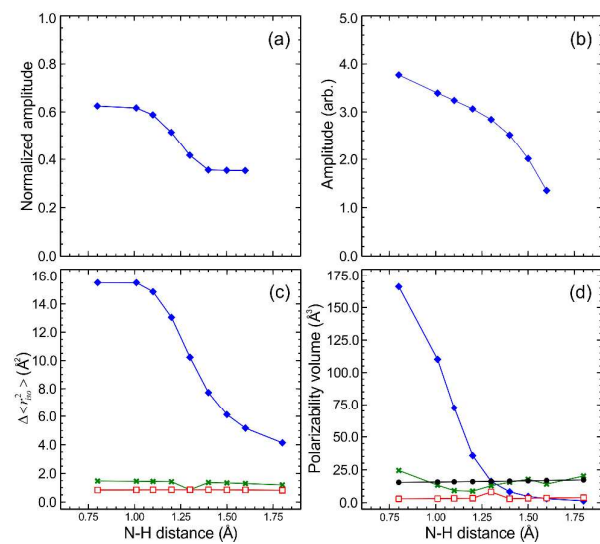
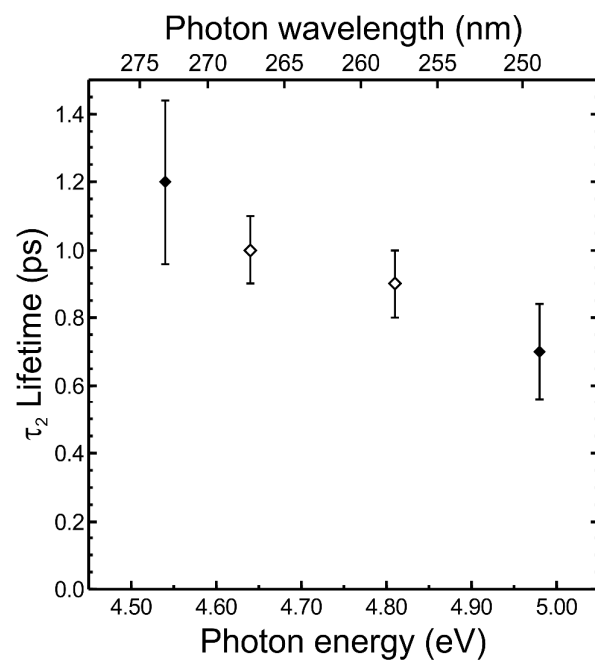
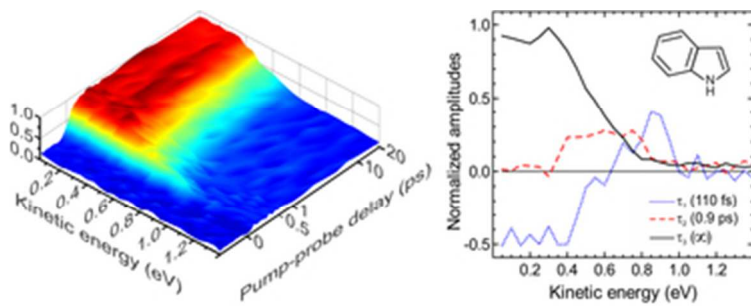


Figure 7





31x12mm (300 x 300 DPI)